SLOVAK UNIVERSITY OF TECHNOLOGY IN BRATISLAVA

Faculty of Electrical Engineering and Information Technology

Reg. No.: 104400-119217

M.Sc. Arif Hussain

Dissertation Thesis Abstract

Multiphysics modelling of superconducting power and magnet applications

Submitted to obtain the academic title of "philosophiae doctor", abbreviated as "PhD."

Study Programme: Physical Engineering

Field of Study: Electrical and Electronics Engineering

External Supervising Institution: Institute of Electrical Engineering, Slovak Academy of Sciences

Thesis Supervisor: Mgr. Enric Pardo, PhD

Bratislava 2025

This thesis was developed in a full-time doctoral study at Institute of Electrical Engineering, Slovak Academy of Sciences, Department of Superconductors, in Bratislava.

Author: **MSc. Arif Hussain**
Institute of Electrical Engineering SAS
Dúbravská cesta 9, 841 04 Bratislava

Supervisor: **Mgr. Enric Pardo, PhD**
Institute of Electrical Engineering SAS
Dúbravská cesta 9, 841 04 Bratislava

Opponents:

doc. Ing. Peter Bokes, PhD.
Slovak University of Technology in Bratislava
Ilkovičova 2961, 841 04 Karlova Ves

Dr.-Ing. Marcela Pekarčíková
Slovak University of Technology in Bratislava
Faculty of Materials Science and Technology in Trnava

Dissertation thesis abstract was sent: 20.05.2025

Dissertation Thesis defence will be held on: 22.08.2025

Dean of faculty, FEI STU: Prof. Ing. Márius Pavlovič, PhD

Contents

1 Introduction

This thesis focuses on multiphysics modeling of High Temperature Superconductors (HTS) for power and magnet applications. The inherent high power-to-weight ratio of superconducting materials makes them attractive for high current density applications. However, it presents complex coupled electromagnetic and thermal challenges that require detailed analysis. Accurate numerical modeling is essential to understand the behavior of HTS devices. The main focus of this PhD thesis is to study thermal quench phenomena in racetrack coils used in high-performance electric motors for aviation applications. This work investigates temperature evolution, hotspot formation, and the effectiveness of cooling strategies. The developed models aid in the safe and efficient design of HTS motor for aviation. This research supports the broader integration of superconducting technologies into power and magnet applications.

2 Summary

HTS have emerged as a promising technology for next-generation electrical machines, especially motors with racetrack coils in the stator, due to their high power density and improved power-to-weight ratio. However, the practical deployment of HTS motors faces critical challenges, most notably the phenomenon of thermal quenching. This refers to the localized loss of superconductivity due to heat generation, which can be triggered by AC losses, short-circuit DC voltages, or screening currents in-

duced during high-frequency operation. These electrothermal instabilities not only compromise motor performance but can also lead to irreversible damage to the superconducting coils if not properly mitigated.

This PhD research focuses on developing a detailed electromagnetic and electrothermal model of HTS racetrack coils for electric motors, especially for hydrogen-electric aircraft. It analyzes coil behavior under normal and fault conditions, including thermal quenches, in both adiabatic and conduction-cooled cryogenic environments (30 K). The study emphasizes the relationship between current density, temperature, and power dissipation to understand the coupled electrothermal dynamics of HTS coils within stators during transient events. The goal is to improve understanding of performance and stability in superconducting motors under extreme conditions.

To achieve this, a robust and computationally efficient software was developed in C++, integrating the Minimum Electro-Magnetic Entropy Production (MEMEP) method for the electromagnetic problem and the Finite Difference Method (FDM) for thermal modeling. The coupled model enables the accurate prediction of electrothermal responses under dynamic operational conditions, providing valuable insights into quench initiation and propagation. The electrothermal model was rigorously benchmarked against the METEP method and other established analytical and numerical techniques, demonstrating strong agreement and reliability.

Through detailed case studies and parametric investigations, this thesis contributes novel understanding and practical tools for the safe design and operation of HTS motors, with a focus

on quench detection, risk mitigation, and thermal management. The findings support the development of next-generation HTS machines that are both high-performing and resilient, paving the way for broader adoption of superconducting technologies in real-world electric power and propulsion systems.

3 Modeling Methods

In practical applications involving complex geometries, analytical methods often fall short in accurately predicting temperature distribution and local current density in superconductors [1]. Numerical modeling techniques, specifically utilized for superconducting properties, are therefore widely used to simulate and analyze their behavior [2]. These approaches offer critical insights for optimizing superconductor performance in real-world applications.

In this work, we develop in-house software for electromagnetic and electrothermal modeling tailored to practical configurations. This custom tool provides optimized speed and efficiency suited to the unique properties of superconductors. Additionally, as our institute owns the software, we are free from licensing constraints, enabling scalable deployment on multiple systems, including supercomputers. This combination of performance and cost-effectiveness supports cutting-edge superconductivity research and fosters innovation in the field.

3.1 Electromagnetic Model: Minimum Electro-Magnetic Entropy Production (MEMEP)

In this work, we model the electromagnetic behavior of the superconducting racetrack coil by the Minimum Electro-Magnetic Entropy Production (MEMEP) method, which is based on a variational principle. This method utilizes a power-law E-J relation that is valid for both 3D and 2D cross-sectional geometries [3, 4]. MEMEP produces encouraging results in the design and optimization of electromagnetic devices [4].

The focus of this PhD thesis is to develop a new modeling tool that utilizes the Minimum Eletro-Magnetic Entropy Production (MEMEP) for the electromagnetic problem and combines it to a thermal model.

There have been other works about variational methods. Similar to the H-formulation proposed by Bossavit [5], there exist other 3D variational formulations [6]. Elliott [7] and Kashima offered a further development of the $H-$formulation. L Prigozhin [8] first proposed a 2D J-formulation for thin superconducting tape or infinitely long wire problems. The Euler-Lagrange formalism for the H-formulation was first presented by Badia [9] and Lopez [10].

Our MEMEP approach in [3] and [4] can be used with power law relation between $\mathbf{J}$ and $\mathbf{E}$, including anisotropic force-free effects. The power-law relation can be written as,

$$\mathbf{E}(\mathbf{J}) = E_c \left(\frac{|\mathbf{J}|}{J_c} \right)^n \frac{\mathbf{J}}{|\mathbf{J}|}, \tag{1}$$

We start with the Maxwell-Faraday differential equation,

$$\nabla \times \mathbf{E} = -\frac{\partial \mathbf{B}}{\partial t} \tag{2}$$

and the relation between vector potential $\mathbf{A}$ and the magnetic field $\mathbf{B}$

$$\nabla \times \mathbf{A} = \mathbf{B}. \tag{3}$$

$$\mathbf{E}(\mathbf{J}) = -\frac{\partial \mathbf{A}_J}{\partial t} - \frac{\partial \mathbf{A}_a}{\partial t} - \nabla\phi, \tag{4}$$

here,

$$\mathbf{A} = \mathbf{A}_J + \mathbf{A}_a \tag{5}$$

where $\mathbf{A}_a$ and $\mathbf{A}_J$ are applied and self vector potential respectively, while ϕ is a scalar potential.

Reference [3] shows that the solution of the differential equation (4), is the minimum of a certain functional, because (4) is the Euler equation of that functional, which is

$$L[\Delta\mathbf{J}] = l \int_S dS \left[\frac{1}{2} \Delta\mathbf{J} \cdot \frac{\Delta \mathbf{A}_J}{\Delta t} + \Delta\mathbf{J} \cdot \frac{\Delta \mathbf{A}_a}{\Delta t} + U(\mathbf{J}_0 + \Delta\mathbf{J}) \right] + VI. \tag{6}$$

where $\Delta\mathbf{J}$ is change in current from the previous time step, $\Delta\mathbf{A}_J$ is change in vector potential due to current density, $\Delta\mathbf{A}_a$ is change in vector potential due to applied field, V is voltage, I is current, $\mathbf{J}_0$ is the current density at time $t - \Delta t$, and the total current density at time t, is $\mathbf{J} = \mathbf{J}_0 + \Delta\mathbf{J}$.

3.2 Electrothermal Model: Finite Difference Discretization

We begin with the general heat diffusion equation, which describes how thermal energy is transferred through a medium over time

$$C_{pv}(T)\frac{\partial T}{\partial t} = \nabla \cdot (\bar{\bar{k}}(T)\nabla T) + p(\mathbf{J}). \tag{7}$$

Above, C_{pv} is the heat capacity per unit volume at constant pressure, $p(\mathbf{J})$ is the power heat density generated by electromagnetic dissipation, which is $p(\mathbf{J}) = \mathbf{E}(\mathbf{J}) \cdot \mathbf{J}$, and $\bar{\bar{k}}$ is the heat capacity tensor that accounts for the material anisotropy. This equation is also valid when $\bar{\bar{k}}$ and C_{pv} are non-homogeneous. We can discretize (7) as detailed in [11] and solve T by the finite difference method. This discretization takes nonhomogeneous heat conductivity and capacity into account. We show temperature dependent heat conductivity $k(T)$ and specific heat $C_{pv}(T)$ of different materials used in our model in table 2, based on the database in [12]. In this work, we discretize the diffusion equation in 2D using the finite difference method (FDM) detailed in [11].

Now, we restrict to infinitely long problems in the z direction. Then, any quantity of the thermal problem does not depend on z, and hence all derivatives in the z direction of (7) vanish. In the FDM, partial differential equations (PDEs) are approximated by replacing the derivatives with finite differences. This process is known as discretization, and it involves dividing the continuous domain into a grid of discrete points, where the value of the solution is approximated at each point as shown in

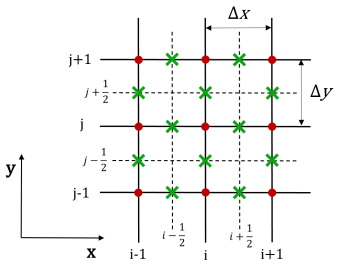

Fig. 1: A 2D uniform grid showing the finite-difference scheme, where the circles (red) are the cell centers and dash lines are the boundaries.

figure 1.

The accuracy of FDM depends on the size of the grid and the finite difference scheme used. The simplest scheme is the forward difference scheme, which uses the value at the current time and the value at the previous time to approximate the derivative. Higher-order schemes, such as the central difference scheme and the backward difference scheme, use more points and produce more accurate approximations. Discretization in FDM is a key step in obtaining a numerical solution to PDEs, and it is extensively used in many fields, including physics and engineering.

When dealing with non-homogeneous heat conductivity in a finite difference method, the coefficients of the discretized equations need to be modified to account for the variation in the

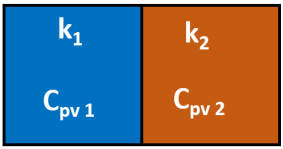

Fig. 2: Sketch of two regions with different heat conductivity, k, and heat conductivity, C_{pv}.

conductivity at the interface between two different materials as can be seen in figure 2. That variation in conductivity could also be caused by a temperature-dependent heat conductivity and two different temperatures. For example, consider the 2D heat diffusion equation with variable conductivity,

$$\frac{\partial T}{\partial t} = \frac{k(T)}{C_{pv}(T)} \left[\frac{\partial^2 T}{\partial x^2} + \frac{\partial^2 T}{\partial y^2} \right] + \frac{p(\mathbf{J})}{C_{pv}}, \tag{8}$$

where $k(T)$ and $C_{pv}(T)$ are non-uniform, temperature dependent, spatial varying thermal conductivity and specific heat capacity respectively. We can discretize these equations in 2D using the following finite difference scheme (see PhD thesis).

$$
\begin{aligned}
T_{i,j}^{n+1} &= T_{i,j}^{n} + \frac{p_{i,j}\Delta t^{n+1}}{C_{pv,i,j}} + \\
&+ \frac{\Delta t^{n+1}}{C_{pv,i,j}\Delta x_{i,j}} \left[k_{x,i+\frac{1}{2},j} \frac{(T_{i+1,j}^{n} - T_{i,j}^{n})}{x_{i+1,j} - x_{i,j}} - k_{x,i-\frac{1}{2},j} \frac{(T_{i,j}^{n} - T_{i-1,j}^{n})}{x_{i,j} - x_{i-1,j}} \right] + \\
&+ \frac{\Delta t^{n+1}}{C_{pv,i,j}\Delta y_{i,j}} \left[k_{y,i,j+\frac{1}{2}} \frac{(T_{i,j+1}^{n} - T_{i,j}^{n})}{y_{i,j+1} - y_{i,j}} - k_{y,i,j-\frac{1}{2}} \frac{(T_{i,j}^{n} - T_{i,j-1}^{n})}{y_{i,j} - y_{i,j-1}} \right],
\end{aligned}
\tag{9}
$$

where $T_{i,j}^{n}$ is the temperature at the center of the cell indexed by (i,j) at time step n, $\Delta t^{n+1} = t^{n+1} - t^{n}$ is the time step between times t^{n} and t^{n+1}, $C_{pv,i,j} = C_{pv}(T_{i,j})$ is the heat capacity at the cell (i,j), $p_{i,j}$ is the dissipated power density at cell (i,j), and $k_{x,i+\frac{1}{2},j}$ and $k_{x,i-\frac{1}{2},j}$ are the thermal conductivity values at the mid-points between grid points i,j and $i+1,j$ and between $i-1,j$ and i,j respectively. Similarly, in the y direction $k_{y,i,j+\frac{1}{2}}$ and $k_{y,i,j-\frac{1}{2}}$ are the thermal conductivity values at the mid-points between grid points i,j and $i,j+1$ and between $i,j-1$ and i,j, respectively. Above we considered the discontinuity of k between neighboring cells. This discontinuity in k can be due to either different materials or a difference of T between neighboring cells. Thus, this finite-difference method enables to take temperature-dependent thermal properties and material discontinuities into account.

Next, we deduce the value of the heat conductivity at the mid points from the heat conductivity at the cells. The most accurate view is to approximate that k is uniform within one cell

(the rectangular region bounded by dash lines in around point (i, j) in figure (1)). Then the heat resistance, R, associated to a heat flux G_x flowing from the center of cell (i, j) to the center of cell $(i+1, j)$ is the sum of heat resistances. The heat resistance is related to the heat conductivity as $R = l/k \cdot S$, where l is the length of the path of the heat flow and S is the cross-section where this heat is flowing. Then, the heat resistance of the heat flux from cell (i, j) to $(i+1, j)$ is, for uniform mesh,

$$R_{i+\frac{1}{2},j} = \frac{1}{2\Delta y_{i,j}\Delta z_{i,j}} \left[\frac{\Delta x_{i,j}}{k_{x,i,j}} + \frac{\Delta x_{i+1,j}}{k_{x,i+1,j}} \right], \tag{10}$$

where $\Delta z_{i,j}$ is the cell size in the z direction, which is the whole length of the studied object for infinitely long problems. From the relation between R and k, we obtain a k related to this heat resistance as

$$k_{x,i+\frac{1}{2},j} = \frac{(\Delta x_{i,j} + \Delta x_{i+1,j})}{2\Delta y_{i,j}\Delta z_{i,j}} \left[\frac{1}{R_{i+\frac{1}{2},j}} \right]. \tag{11}$$

As a result, the heat conductivity associated to the mid-point between cell (i, j) and $(i+1, j)$ is,

$$k_{x,i+\frac{1}{2},j} = (\Delta x_{i,j} + \Delta x_{i+1,j}) \left[\frac{\Delta x_{i,j}}{k_{x,i,j}} + \frac{\Delta x_{i+1,j}}{k_{x,i+1,j}} \right]^{-1}. \tag{12}$$

The resulting numerical solution of T_{ij}^{n+1} from a known $T_{i,j}^{n}$ at all cells can be obtained by (9) using the mid-point conductivities (or conductivities at the cell surfaces) from (12). The reader should keep in mind that the heat conductivity at the half points of the edges, is calculated from $k_{x,ij}$ at the cell.

3.2.1 Stability condition

A stability condition is a mathematical requirement that has to be met in finite difference numerical simulations of heat diffusion so that the numerical solution stays correct and does not diverge over time. This condition is known as the Courant-Friedrichs-Lewy (CFL) stability condition [13]. The CFL stability criterion may be written mathematically as:

$$\Delta t \leq \frac{1}{2}\min(C_{pv}\Delta x^2/k_x, C_{pv}\Delta y^2/k_y) \tag{13}$$

where Δt is the time step size, Δx and Δy are the grid spacing in the x and y direction respectively, "min" refers to the minimum among all the cells of the sample, and $C_{pv}(T)$ is the heat capacity per unit volume and k_x is the thermal conductivity in horizontal direction, and k_y the thermal conductivity in vertical direction of the sample. The numerical solution will become unstable if this requirement is not met, and the simulation will not adequately reflect the actual behavior of the superconductor.

3.3 Coupling of Electromagnetic and Electro-Thermal models

The coupling of electro-thermal and electro-magnetic models is crucial for accurately analyzing superconductors under varying operating conditions. This work employs an *indirect coupling technique* using separate solvers: the Finite Difference Method (FDM) for electro-thermal problems and the Minimum Electro-Magnetic Entropy Production (MEMEP) method for electro-

magnetic analysis. These solvers are linked within a time evolution loop, where FDM is executed first in each time step to update the temperature-dependent critical current density $J_c(T)$. The MEMEP solver then computes the current density J_z and power loss $p(J_z)$, which is fed back to the FDM solver. This iterative process continues until convergence is achieved, enabling a comprehensive simulation of superconducting power applications.

3.4 Homogenized material properties

We consider the homogeneous model for the electric and thermal properties of the superconducting tape because it also contains layers of several materials with very different properties, as shown in figure 3(b). This simplifies the complexity of the problem while still capturing the essential behavior. For the electric properties, we consider that all the materials are connected in parallel, and hence the effective resistivity is

$$\rho_e = \left[\sum_{i=1}^{n} \frac{S_m}{S \rho_m} \right]^{-1} \tag{14}$$

where S is total tape section, S_m is the section of each material, ρ_m is the resistivity of the material, and n is the number of different materials. In addition, superconductors presents the non-linear resistivity associated to the power-law relation. Actually, the superconducting layer itself also contains normal conducting electrons in parallel. This contribution to the effective resistivity is considered as an additional layer.

The homogenized thermal properties of the superconducting tapes, which is obtained from C_{pv}, k_x, and k_y at each material of the tapes. The effective quantities are

$$C_{pv,e} = \frac{1}{S} \int C_{pv}(x,y)\, dxdy \tag{15}$$

$$k_{x,e} = \frac{1}{D_y} \int dy \left[\frac{1}{D_x} \int d_x \frac{1}{k_x(x,y)} \right]^{-1} \tag{16}$$

$$k_{y,e} = \frac{1}{D_x} \int dx \left[\frac{1}{D_y} \int d_y \frac{1}{k_y(x,y)} \right]^{-1} \tag{17}$$

where D_x and D_y are the tape sizes in x and y directions respectively including the isolation layer between tapes.

3.5 Temperature dependence of J_c

The critical current density exhibits a strong temperature dependence. The temperature dependence of $J_c(T)$ close to the critical temperature, T_c can be described by an expression that is valid for temperatures of 77 K and above [14]. The temperature dependence of power law $\mathbf{E}(\mathbf{J})$ relation (1) can be re-written as

$$\mathbf{E}(\mathbf{J}) = E_c \left(\frac{|\mathbf{J}|}{J_c(T)} \right)^n \frac{\mathbf{J}}{|\mathbf{J}|}, \tag{18}$$

where,

$$J_c(T) = J_c(T_l)\,\frac{T_c - T}{T_c - T_l}, \tag{19}$$

where, T_c is the normal-state transition temperature and T_l is the initial temperature. Naturally, when $T \geq T_c$, $J_c = 0$.

4 Results and Discussion

This thesis presents a detailed study of the electrothermal behavior of HTS racetrack coils in superconducting motors, for both regular AC operation and transient fault conditions. The analysis begins under adiabatic conditions and later includes the effects of cooling. We considered 77 K for initial studies and proof-of-concept demonstrations, as well as for comparison with available experimental data, whereas 30 K was chosen as it represents a relevant cryogenic temperature for superconducting motors in aviation applications.

4.1 Liquid Nitrogen Operation (77 K)

4.1.1 Studied Configuration

Here, a specialized tape configuration comprising REBCO superconductor, silver, hastelloy, and stycast is employed in racetrack coils for superconducting motors (figure 3). Stycast serves as an electrical insulator between the turns. The silver layer

is critical for oxygenation during processing and improves thermal conduction due to its high thermal conductivity. Superconductivity at cryogenic temperatures is achieved through the REBCO layer.

The coil's performance depends on key material properties such as critical current density (J_c) and critical temperature (T_c). In this case we assume, $T_c = 92\,\mathrm{K}$ and $J_c = 1.875 \times 10^{10}\ \mathrm{A\,m^{-2}}$. The thermal behavior is governed by heat capacity per unit volume (C_{pv}) and thermal conductivity (k). The metallic components (silver, hastelloy) and electrical insulator play vital roles in heat and electrical transport.

Electrical characteristics are further influenced by the normal-state resistivity of the superconductor and the resistivities of the metallic constituents, which are summarized in table 1. These factors affect the dissipation in normal state and the coil current under DC fault voltage. The normal-state resistivity and resistivity of the metals do not affect the efficiency, since they only play a role when the superconductor is at temperature above T_c.

To optimize racetrack coil performance and reliability in motor applications, careful consideration of geometry and cooling is essential. The reference coil used in this study has 30 turns, an inner bore diameter of 50 mm, and a straight section length of 20 cm.

While the coils primarily operate in an AC regime, they may occasionally be subjected to high DC voltages due to transient faults in power source. These fault scenarios can lead to significant current flow and temperature rise, which must be accurately evaluated to ensure the safe and reliable performance of

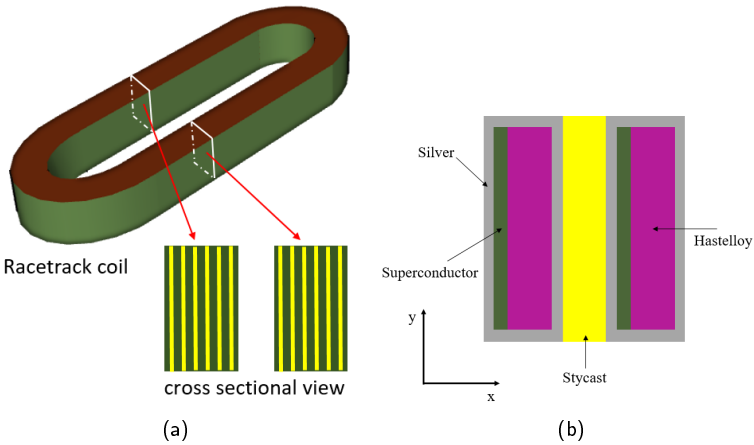

Fig. 3: (a) Sketch of a racetrack coil and its cross-section. In the cross-section the green part represents the superconducting tape with all its layers and the yellow part is the electric insulation. (b) Cross-sectional view of two neighboring superconducting turns with tycast insulation in between.

Metallic layers	thickness [μm]	ρ [Ωm]	C_p [$\mathrm{Jkg^{-1}K^{-1}}$]	C_{pv} [$\mathrm{Jm^{-3}K^{-1}}$]	k [$\mathrm{Wm^{-1}K^{-1}}$]
Silver	2	1×10^{-8}	235	2.46×10^{6}	400
Stycast	50	1×10^{13}	138.6	3.17×10^{5}	0.8
REBCO	2	3×10^{-7}	156.65	1×10^{6}	9
Hastelloy	100	120×10^{-8}	425	3.7×10^{6}	7

Tab. 1: Physical properties of the materials in the superconducting tape for our model [15].

the coil. Now we only discuss AC voltage conditions for normal motor operation, however, we detailed the transient fault conditions (short-circuit DC voltage) both adiabatic and cooling in the thesis.

The initial analysis focuses on AC and DC voltage conditions at 77 K, the boiling temperature of liquid nitrogen, to support early-stage design and conceptual validation. Operating at this temperature allows for practical experimentation, as liquid nitrogen offers a convenient and cost-effective cooling solution for laboratory studies.

4.1.2 100 V AC: Adiabatic

An interesting phenomenon has been seen when an alternating voltage of 100 V amplitude and 500 Hz frequency is applied to the racetrack coil while it is operating under adiabatic conditions (figure 4a). The current begins from zero to its maximum value sinusoidally, which remains below I_c (figure 4b), and the temperature rises slowly. The average temperature presents plateaus

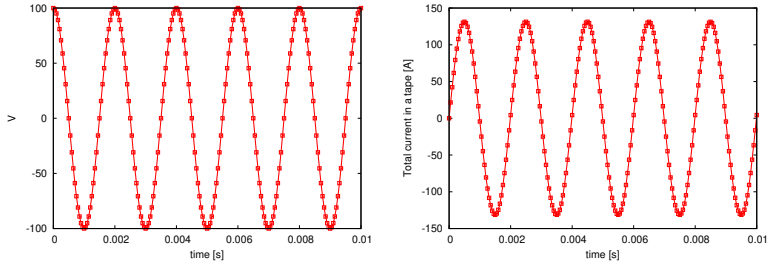

(a) Alternating voltage input of 100 V (b) Output current

Fig. 4: (a) Alternating voltage input of 100 V (b) Total current in racetrack coil for 100V amplitude of alternating voltage with no heat exchange with the cryogenic liquid with initial temperature of 77 K.

followed by a rise in temperature. The maximum rate, dT/dt, occurs when the dissipation ($P \equiv l \int_S dS\, \mathbf{J} \cdot \mathbf{E}$) is maximum, while the plateaus correspond to dissipation minima. This explains why the time spacing between plateaus is half the voltage period, since the dissipation periodicity is the same as the input power $P_{\text{in}} \equiv VI$. Actually, the dissipation will have a phase shift with the input power because of inductive effects, which cause periodic changes in magnetic energy. In our case, the peak or valley of the voltage corresponds to the end of the plateaus in the temperature.

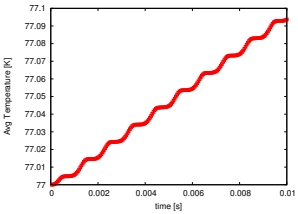

Fig. 5: Average temperature in the racetrack coil for 100V amplitude of alternating voltage with no heat exchange with the cryogenic liquid with initial temperature of 77 K.

4.1.3 1000 V AC: Adiabatic

When a 1000V AC is applied to the racetrack coil, a different scenario unfolds. The current abruptly surges beyond the critical current I_c, and consequently, the temperature rises sharply which is nearly equal to critical temperature (T_c) at 5ms (Figure 6, 7). Therefore, such high voltages should be avoided in this coil. This rapid increase in temperature poses a significant challenge and necessitates the design and implementation of an efficient cooling mechanism or a very fast-response switch to disconnect the large voltage to prevent thermal damage to the superconductor. In usual operation, the coil will not be submitted to such high voltages. However, these high voltages might occur due to faults in the electric system. To overcome this effect, the cooling mechanism must effectively dissipate or absorb the heat generated by the elevated current, ensuring that the temperature remains within safe operating limits at least until

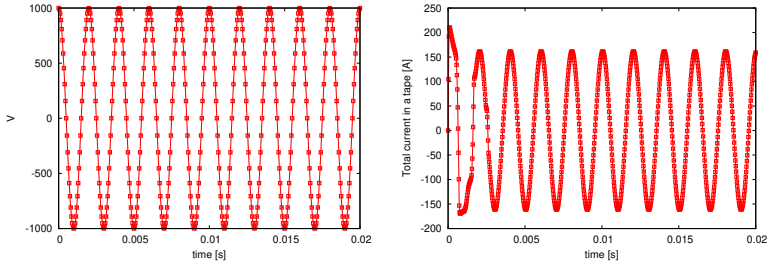

(a) Alternating voltage input of 1000 V (b) Output current

Fig. 6: (a) Alternating voltage input of 1000 V (b) Total current in racetrack coil for 1000V amplitude of alternating voltage with no heat exchange with the cryogenic liquid.

a circuit breaker can disconnect the high voltage from the coil. Instead, we could install a superconducting fault current limiter in series with the coil, since the response of that device is also very fast.

4.2 Low Temperature Operation (30 K)

4.2.1 Studied Configuration

In this study, we use a realistic REBCO-based tape configuration, which consists of REBCO layer, silver, stainless steel, and polyimide (Kapton) for racetrack coils in superconducting

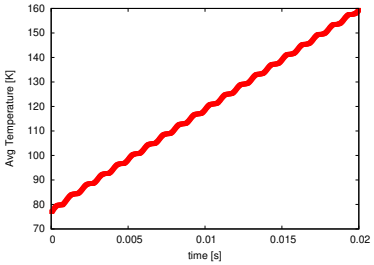

Fig. 7: Cross-section average temperature in racetrack coil for 1000V amplitude of alternating voltage with adiabatic conditions.

motors. In this design, we replace the materials used in the previous tape dimensions in figure 3. We use polyimide (Kapton) instead of Stycast, and stainless steel replaces Hastelloy for structural components. Polyimide serves as electrical insulation between turns, differing slightly from previous setups. The analysis considers key material properties, including a critical temperature $T_c = 92\,\mathrm{K}$ and critical current density at 30 K of $J_c = 5.875 \times 10^{10}\ \mathrm{A\,m^{-2}}$ (19). For the geometric parameters, we consider using a 30 turn coil with a 50 mm inner bore and 20 cm straight segment length.

In this study, we investigate the impact of conduction cooling applied from the top surface of the racetrack coil on its thermal stability and overall performance, particularly under fault conditions. To achieve this, a thin 10-micron layer of polyimide (Kapton) is placed on the top of the coil, with the temperature

Temperature [K]	Silver		Stainless Steel		Polyimide (Kapton)	
	k [W/m.K]	C_{pv} $[J/(kg \cdot K)]$	k [W/m.K]	C_{pv} $[J/(kg \cdot K)]$	k [W/m.K]	C_{pv} $[J/(kg \cdot K)]$
30	1930	54.392	3.468	30.539	0.067	116.229
40	1050	89.161	4.670	58.687	0.083	172.862
50	700	118.365	5.730	95.690	0.097	224.323
60	550	139.745	6.646	136.915	0.108	270.398
80	471	170.246	8.114	215.259	0.128	348.942
100	450	190.623	9.223	275.496	0.141	413.687
200	430	225.726	12.632	416.429	0.174	626.773
300	429	237	15.308	469.449	0.192	754.550

Tab. 2: Thermal properties of the materials in the superconducting tape for our model, where $C_{pv} = \rho_m \cdot C_p$, and ρ_m is the density of each material.

on its surface carefully maintained at 30 K throughout the process (Figure 10). This simulates conduction cooling from one side.

We adopt a homogenized approach for modeling the electromagnetic and electrothermal behavior of superconducting tapes, as detailed in prior works [11, 15, 16] (see section 3.4). For thermal analysis, temperature-dependent properties such as volumetric heat capacity ($C_{pv,e}$) and thermal conductivities ($k_{x,e}$, $k_{y,e}$) are calculated using weighted averages across the layered structure of the tape.

4.2.2 100 V DC short circuit: Adiabatic

when a short-circuit of 100 V magnitude occurs in the racetrack coil, the current initially rises sharply overcoming the critical current, and then it decreases following noticeable drops to a

stable value (Figure 8). As we detail in the next paragraph, this behavior is accompanied by rapid temperature rise, which results in a transition of a few turns of the coil from the superconducting to the normal state (Figure 9(a,b)). As a result, heat generated in these turns begin diffusing into neighboring turns, leading to observable drops in current (Figure 8).

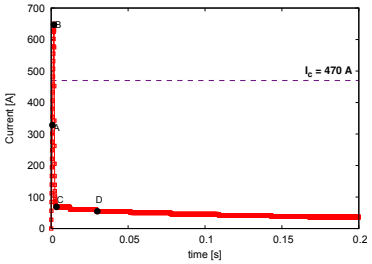

Fig. 8: Total current in racetrack coil for 100 V DC input with no heat exchange with its surroundings.

4.2.3 100 V DC short circuit: Conduction cooling

In this work, we explore that how conduction cooling from the top surface enhances the performance of the racetrack coil by placing a thin 20-micron polyimide (Kapton) layer on top and maintaining its surface temperature at 30 K. Here, we simulate one-sided (from top) conduction cooling (Figure 10).

At 100 V, rapid temperature rise is observed after the initial current ramp (figure 11 and 12), which is due to high Joule

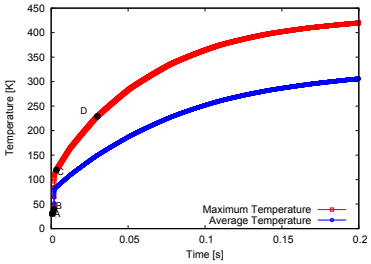

Fig. 9: Temperature rise in racetrack coil for 100 V DC input with no heat exchange with the cryogenic liquid.

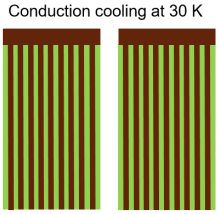

Fig. 10: Sketch of the cross section of the racetrack coil with cooling from the top, where green color represents superconductor with all metallic layers, and red color represents polyimide (kapton) insulation layer.

heating ($p = \mathbf{J} \cdot \mathbf{E}$) caused by net current overcoming the critical current at part of the coil. However, the fixed cooling boundary condition (figure 10) effectively extracts the generated heat, resulting in temperature stabilization after approximately 0.8 s (figure 12). This stabilization indicates that the top-surface cooling counteracts the heat generated in the coil, preventing permanent damage due to overheating, which could occur above 400 K.

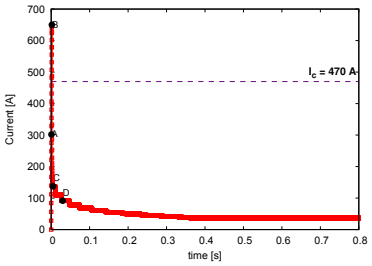

Fig. 11: (a) Total current in racetrack coil for 100 V DC input with with cooling from the top at 30 K.

Next, we detail the temperature, current density, and power distributions (see figure 13). At the initial ramp and up to the current peak the temperature, current density, and power density is qualitatively the same as without cooling (figure 13(a,b,c,d,e,f)). The effect of cooling is still not appreciable because of the short elapsed time. At the first current drop, temperature in the central turns is above T_c except the top surface of the coil where cooling is imposed. Over the time, the impact of cooling from

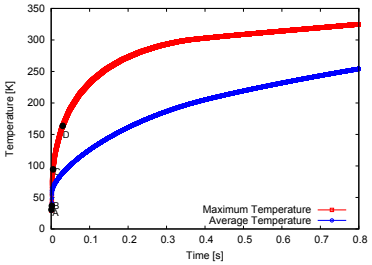

Fig. 12: (a) Temperature rise in racetrack coil for 100 V DC input with cooling from the top at 30 K.

the top becomes apparent, as the temperature profile stabilizes under the influence of the fixed cooling boundary (see temperature profiles in figure 13(a,d,g,j)). The cooling mechanism avoids thermal runaway, which keeps the maximum temperature well below 400 K, and hence preventing thermal damage. However, the temperature at the central turns is still well above T_c. As for the case of no cooling, the current presents several drops caused by the expansion of the normal zone at the center of the coil. Each drop corresponds to the expansion of the normal zone to an additional turn.

4.2.4 1 V DC short circuit: Conduction cooling

We analyze the electromagnetic and thermal response of the racetrack coil under a 1 V DC short-circuit condition with conduction cooling applied only from the top surface at 30 K. Dur-

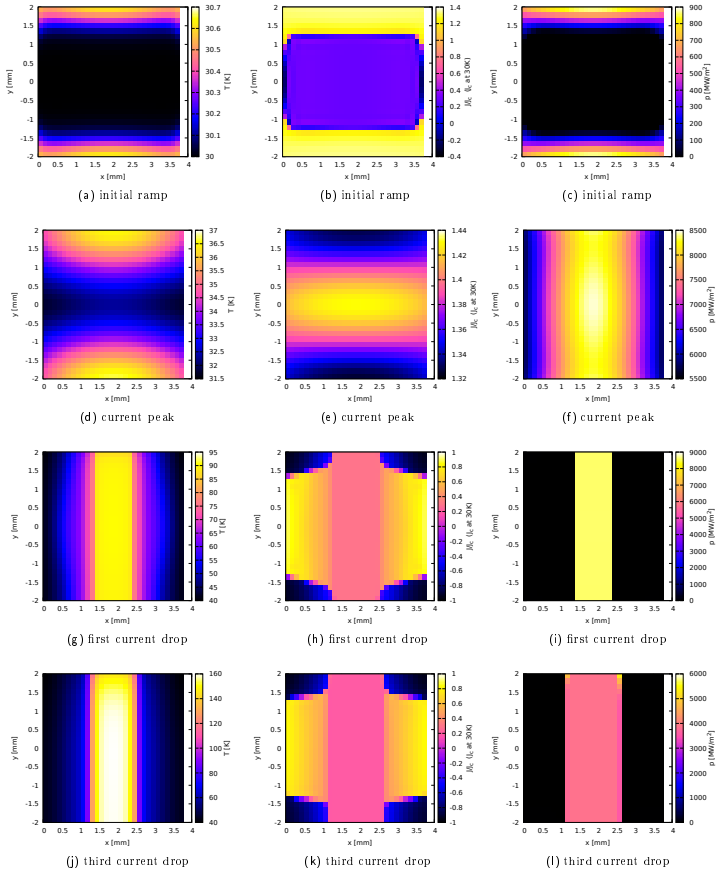

Fig. 13: Coil cross-section showing maps of temperature (left), current density (middle), and power loss density (right) for top cooling at 100 V amplitude of DC voltage for different times: (a,b,c) at point A, (d,e,f) at point B, (g,h,i) at point C, and (j,k,l) at point D in figures 11 and 12.

ing the initial current ramp (point A in figure 14), the current rises gradually due to the coil's inductance and low voltage. When the current exceeds the critical current $I_c = 470\,\mathrm{A}$ (point B), localized heating causes a transition to the normal state, resulting in a sudden increase in resistance and temperature (point C), followed by a drop in current. The coil then enters a self-oscillatory region (points D–F and beyond), where current and temperature fluctuate periodically (Figures 14 and 15). These oscillations arise from a feedback loop: local heating causes resistive regions that reduce current; the lower current decreases Joule heating, allowing cooling and partial restoration of superconductivity; current then rises again, repeating the cycle. This behavior highlights the interplay between superconducting transitions, inductive effects, and anisotropic heat transfer.

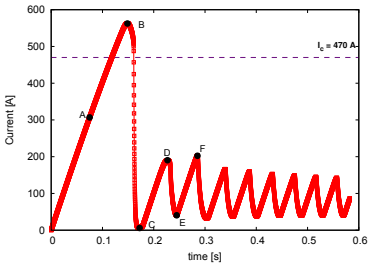

Fig. 14: (a) Total current in racetrack coil for 1 V DC input with cooling from the top at 30 K.

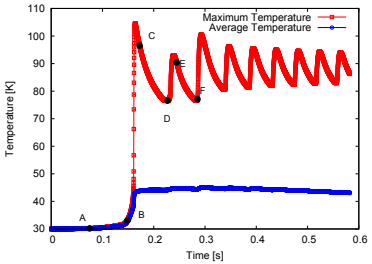

Fig. 15: (a) Temperature rise in racetrack coil for 1 V DC input with cooling from the top at 30 K.

4.3 Higher thermal conducting inter-layer

In this study, we examine the revised geometry incorporating tape-to-tape insulation with enhanced thermal conductivity, which is set to that of stainless steel for testing purposes. The metallic substrate thickness is reduced from 100 μm to 80 μm to reflect a more compact and thermally responsive design. We analyze the 1 V case and consider both adiabatic and conduction cooling conditions to investigate the temperature evolution and current fluctuation under these revised conditions. We chose these parameters in order to observe high oscillations. Here we only discuss conduction cooling, however, we study adiabatic condition as well in the thesis.

4.3.1 Conduction Cooling

Now when short-circuit of 1 V amplitude occurs in the racetrack coil, it exhibits completely periodic thermal and current behaviors (figure 16 and 17). After the peak of current (figure 16 point B), we observe a sharp rise in temperature due to non-linear Joule heating. This is followed by a drop in maximum temperature and a subsequent temperature rise, creating a cyclic pattern (figure 17). The cooling mechanism from the top surface plays a crucial role in avoiding thermal damage of the superconductor and also causes perfectly periodic oscillations of temperature and current after a transient, which extends to the third temperature peak. However, at certain point a circuit breaker should act in order to avoid mechanical fatigue due to cyclic thermal stress. Indeed, temperature oscillations have high amplitude, where the maximum temperature ranges from around 30 to 280 K at a rate of roughly 6 times per second.

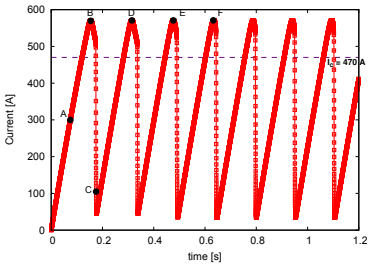

Fig. 16: Total current in racetrack coil for 1 V DC input with with cooling from the top at 30 K.

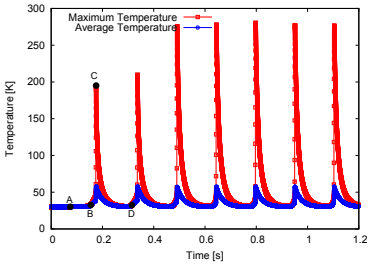

Fig. 17: Temperature rise in racetrack coil for 1 V DC input with cooling from the top at 30 K.

5 Conclusions

In this thesis, we study the impact of DC and AC voltages on racetrack coils under various cooling conditions such as adiabatic, liquid nitrogen (77 K), and conduction cooling (30 K). Under liquid nitrogen bath (at 77 K), we have found that low DC voltages (e.g., 0.1 V) are safe, while very high DC voltages (1000 V) cause rapid quenching and thermal damage to superconductor. Intermediate voltages (10–100 V) show unclear long-term effects but cooling can help to avoid damage. For AC, low voltages (100 V) cause manageable temperature rises, but high voltages (1000 V) lead to quick overheating beyond critical limits.

Under conduction cooling at 30 K, 100 V DC causes quenching without permanent damage, but 1000 V leads to thermal damage similar to adiabatic cases. At 1 V DC, cyclic oscillations in current and temperature occur, which is enhanced when considering higher thermal conductivity between coil turns.

These findings demonstrate that under conduction cooling at 30 K, which is relevant to electric motor applications in aviation, the analyzed racetrack coils can withstand fault-level DC voltages of at least 100 V without incurring irreversible thermal damage, which highlights their robustness for integration into next-generation superconducting propulsion systems.

References

References

[1] F. Grilli, E. Pardo, A. Stenvall, D. N. Nguyen, W. Yuan, and F. Gömöry. Computation of losses in HTS under the action of varying magnetic fields and currents. IEEE Trans. Appl. Supercond., 24(1):8200433, 2014.

[2] E. Pardo and F. Grilli. Numerical Modeling of Superconducting Applications. World Scientific, 2023.

[3] E. Pardo and M. Kapolka. 3D computation of non-linear eddy currents: Variational method and superconducting cubic bulk. Journal of Computational Physics, 344:339–363, 2017.

[4] E. Pardo, J. Šouc, and L. Frolek. Electromagnetic modelling of superconductors with a smooth current-voltage relation: variational principle and coils from a few turns to large magnets. Supercond. Sci. Technol., 28:044003, 2015.

[5] A. Bossavit. Numerical modelling of superconductors in three dimensions: a model and a finite element method.

[6] A. Bossavit. Whitney forms: a class of finite elements for three-dimensional computations in electromagnetism. IEE Proceedings A, 135(8):493–500, 1988.

[7] C.M. Elliott and Y. Kashima. A finite-element analysis of critical-state models for type-II superconductivity in 3D. JMA, 27:293–331, 2006.

[8] V. Sokolovsky, L. Prigozhin, and J. W. Barrett. 3D modeling of magnetic atom traps on type-II superconductor chips. Supercond. Sci. Technol., 27(12):124004, 2014.

[9] A. Badía-Majós and C. López. Modelling current voltage characteristics of practical superconductors. Supercond. Sci. Technol., 28(2):024003, 2015.

[10] Guilherme G Sotelo, Felipe Sass, Miquel Carrera, Josep Lopez-Lopez, and Xavier Granados. Proposal of a novel design for linear superconducting motor using 2g tape stacks. IEEE Transactions on Industrial Electronics, 65(9):7477–7484, 2018.

[11] A Hussain, A Dadhich, and E Pardo. Thermal quench modeling of REBCO racetrack coils under either alternating current or short-circuit voltage. Superconductor Science and Technology, 37(11):115028, oct 2024.

[12] National Institute of Standards and Technology |orig-date=january 15, 2025 |access-date=2025-01-15. `https://trc.nist.gov/cryogenics/materials/materialproperties.htm`.

[13] Hans Petter Langtangen and Svein Linge. Finite Difference Computing with PDEs : A Modern Software Approach. Springer Open, 2010.

[14] Enric Pardo and Anang Dadhich. Electro-thermal modelling by noval variational mehtod: racetrack coil in short-circuit. IEEE Transactions on Applied Superconductivity, 33(5):17, 2023.

[15] Enric Pardo and Anang Dadhich. Electro-thermal modelling by novel variational methods: racetrack coil in short-circuit. IEEE Trans. Appl. Supercond., 33(5):5201606, 2023.

[16] Anang Dadhich, Philippe Fazilleau, and Enric Pardo. A novel and fast electromagnetic and electrothermal software for quench analysis of high field magnets. Supercond. Sci. Technol., 2024. doi:10.1088/1361-6668/ad68d3.